RSC Advances

PAPER

View Article Online
View Journal | View Issue

Cite this: *RSC Adv.*, 2026, **16**, 9692

Mechanochemical solid-state synthesis of Pd-based catalysts with tunable size effects for Suzuki–Miyaura coupling reaction

Zizo Feketshane,[a] Banele Vatsha *[a] and Ndzondelelo Bingwa *[b]

Received 1st January 2026
Accepted 11th February 2026

DOI: 10.1039/d6ra00004e

rsc.li/rsc-advances

Palladium catalysts are widely used in the Suzuki–Miyaura cross-coupling reaction; however, their high cost and scarcity demand strategies to reduce Pd usage without compromising catalytic performance. In this study, we report supported Pd catalysts with low loading, prepared by the ball milling method, an eco-friendly and efficient route to highly active catalysts. These low-loading Pd catalysts were supported on alumina (Al_2O_3), silica (SiO_2), and titania (TiO_2). The influence of support properties on catalytic performance in the Suzuki–Miyaura coupling reaction was systematically investigated. In this work all Pd catalysts exhibit good thermal stability with less than 10% weight loss at 1000 °C. They have high surface areas ranging between 20.6 ± 1.0 to 296 ± 15 $m^2\ g^{-1}$. Diffuse Reflectance Ultraviolet-Visible (DR-UV-Vis) spectroscopy indicated that smaller clusters have altered redox potentials; their electron density changes due to introduction of discrete, redox-active states that strongly couple with the oxide support. A comparison was made between the solution-phase and solid-phase methods for the Suzuki–Miyaura reaction. The catalysts exhibited excellent catalytic activity, achieving up to 97% substrate conversion within one hour at room temperature *via* the mechanochemical route. These catalysts also showed good reusability for at least four catalytic cycles without losing significant activity. Therefore, our study offers an eco-friendly method to develop highly stable Pd-based catalysts for efficient catalytic Suzuki–Miyaura reaction.

1. Introduction

The Suzuki–Miyaura coupling reaction, is an organic synthesis route that typically employs palladium (Pd) catalysts to facilitate the carbon–carbon (C–C–) cross-coupling of aryl halides with boronic acids.[1] Palladium, due to its unique ability to facilitate the cross-coupling of organohalides and organoboranes, is regarded as a highly efficient catalyst for these kinds of reactions.[2–4] However, the high commercial value of Pd and the high synthesis cost of Pd-based catalysts have been their limitation for wide-scale application.[5] To address these issues, the exploration of the bulk reduction to nanoparticles or ultrasmall clusters for use as catalysts is still an interesting investigation.[6] Even recent studies are still showing the intriguing size-dependent catalytic activity of metals, specifically in the context of reducing bulk metal to nanoparticles, single atoms, or small clusters. Also, the efficiency and impact of bulk reduction of active metal phases on selectivity trends in a variety of reactions is a topic of interest.[7,8] Zhang *et al.* recently reported the effect of metal size in hydrogenation reactions; correlating the metal size effect showed that the overall TOF decreased as the average Pt particle diameter increased, thus suggesting a strong size-dependence of catalytic activity, with smaller particles exhibiting higher activity due to a higher surface-to-volume ratio of surface atoms. Therefore, exposing more active surface atoms relative to their total number of atoms enhances catalytic activity.[9] Zhaolu *et al.* investigated the effect on catalytic activity, selectivity, and stability of different sizes of supported Pd particles; they found that with the reduction in particle size, there was an enhancement of the BET surface area, leading to high catalytic activity.[10]

The reduction in metal size can drastically alter the electronic structure and catalytic behavior of the catalyst, influencing the reaction kinetics and mechanism of the Suzuki coupling process.[11] Single atom and small cluster types of catalysts provide a new and exciting opportunity to improve the performance of heterogeneous catalysts.[12] Not only are these minimalist catalysts allowing for full utilization of the expensive precious metals, but the metal also inherits different properties, leading to enhanced activity and selectivity for several reactions.[13] However, the synthesis of ultrasmall cluster catalysts and nanoparticles is still challenging.[14] The ultrasmall cluster catalysts or nanoparticles tend to migrate and aggregate into larger particles during their synthesis or under harsh reaction conditions, making it difficult to maintain their isolated state or

---

[a] *Research Centre for Synthesis and Catalysis, Department of Chemical Sciences, University of Johannesburg, P. O. Box 542, Auckland Park, 2006, Johannesburg, South Africa. E-mail: bvatsha@uj.ac.za*

[b] *Institute for Catalysis and Energy Solutions (ICES), College of Science, Engineering and Technology, University of South Africa, Florida Science Campus, Roodepoort, 1709, South Africa. E-mail: bingwns@unisa.ac.za*

uniform size. It is difficult to achieve uniform dispersion of metals on catalytic support, and it is also hard to scale up reproducibly. Different approaches, such as hydrothermal, sol–gel, wetness co-impregnation, atomic layer deposition, and physical vapor deposition, have been employed in their synthesis.[15–17] While these methods allow fine control over particle size, mechanochemical synthesis offers solvent-free conditions, reduced energy input, and scalability.[18]

Recently, mechanochemistry, often referred to as the ball-milling method, has captured the attention of many researchers for the fabrication of heterogeneous catalysts because of its distinct advantages centred around eco-friendliness, scalability, and a wide application scope.[19] However, despite these advantages, mechanochemical methods may present challenges, such as limited control over particle size distribution and potential structural modification of the support. Therefore, understanding how mechanochemical synthesis influences metal dispersion, surface properties, and catalytic performance remain essential.[20–22] In mechanochemical synthesis, mechanical energy is generated in the ball milling apparatus, where the movement of the grinding bowl generates kinetic and potential energy in the grinding balls and material loaded inside it to reconstruct chemical bonds of the new material. This method is affected by several milling parameters, such as grinding ball size, time, and speed or frequency of the milling process, to mention a few.[23–25]

Herein, we report a highly efficient and pollution-free ball milling method for the direct synthesis of low loading ultra-small clusters of palladium (Pd_1) and nanoparticles (Pd_n) supported on different catalyst supports (Al_2O_3, SiO_2, and TiO_2). We aim to study the size effect induced by the solid-state mechanochemical synthesis of the catalysts in the green Suzuki–Miyaura reaction at mild temperatures.

2. Experimental section

2.1 Materials

All chemicals were purchased from commercial suppliers and used as received without any further purification. Potassium tetrachloropalladate(II) (K_2PdCl_4, >99%), sodium borohydride ($NaBH_4$, (>98%)), phenylboronic acid ($C_6H_7BO_2$, 95%), bromobenzene ($C_6H_5Br \geq 99.5\%$), tetraethyl orthosilicate (TEOS (SiO_2 content: 28–28.8%)), pluronic P123 ($EO_{20}PO_{70}EO_{20}$, > 98%), decane ($C_{10}H_{22}$, > 99.9%), aluminum hydroxide ($Al(OH)_3$, > 99%), and titanium isopropoxide ($T_i[OCH(CH_3)_2]$ (Ti content: 27.8–28.6%), hydrochloric acid (HCl (32%)), NMR solvent: chloroform-*d* ($CDCl_3$) (99.8%), methanol (99.5%), ethanol (>99%), isopropanol (>99.5%), butanol (>99%), dichloromethane (DCM (>99.9%)), barium sulfate ($BaSO_4$ (>99%)) dimethylformamide (DMF (>99.8%)), and sodium carbonyl anhydride (Na_2CO_3), (>99.9%) were all purchased from Merck Chemicals, RSA.

2.2 Catalysts synthesis protocol

Supported ultrasmall Pd clusters (Pd_1) and nanoparticles (Pd_n) catalysts were prepared using vibratory ball milling (liquid-assisted grinding (LAG)). LAG is empirically characterized by η as shown in eqn (1).

$$\eta = \frac{V}{m} \tag{1}$$

where η is the ratio of liquid volume to sample weight and V is the volume of the liquid in microliters (μL) and m is the mass of the reagents.[26] For the synthesis of ultrasmall Pd clusters, a 0.60 g mass of the support (Al_2O_3, SiO_2, or TiO_2), and stoichiometric amounts of potassium tetrachloropalladate (0.1 wt% or 1.0 wt% Pd) were mixed. A 0.06 ml mixture of HCl (37%) and H_2O ($V_{HCl} : V_{water} = 1:1$) was added to an agate grinding jar. The mixture was placed into a vibratory ball mill at 25 Hz for 30 minutes, then the product was calcined at 400 °C for 3 hours. The synthesis of nanoparticles followed the same procedure as that of ultrasmall Pd clusters. The sample's stoichiometric amounts of palladium acetate were 1 wt% and 5 wt% Pd, and instead of adding HCl, 0.05 mol of urea and 0.05 mol $NaBH_4$ were added to achieve the reduction of Pd cations to Pd^0. Thereafter, the synthesized catalysts were characterized using various techniques described in the SI.

2.3 Catalytic evaluation: Suzuki–Miyaura cross-coupling reaction

The catalytic performance of the synthesized catalysts was evaluated in the Suzuki coupling reaction, and a comparison between the conventional oil-bath heating (solution state set-up) and mechanochemistry (solid state set-up) methods was done, see Scheme 1. A catalytic performance evaluation using bromobenzene and phenylboronic acid as standard substrates and a base (Na_2CO_3) in the coupling reaction was undertaken. For both catalyst synthesis methods, control reactions were conducted without any catalysts, and no product yield was detected. The percentage conversion of the substrate was determined using eqn (2).

$$\%\ \text{Conversion} = \frac{\text{moles}_{\text{substrate}(0)} - \text{moles}_{\text{sustrate}(t)}}{\text{moles}_{\text{substrate}(0)}} \times 100 \tag{2}$$

where $\text{moles}_{\text{substrate}(0)}$ is the initial moles of bromobenzene and $\text{moles}_{\text{substrate}(t)}$ are the final moles of bromobenzene at any given time.

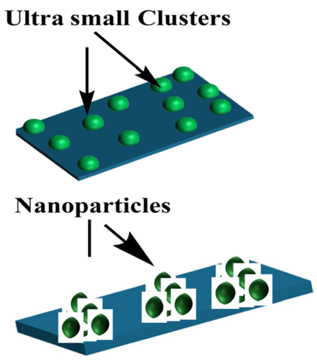

Scheme 1 Proposed MSI of atomically dispersed ultra-small clusters (Pd_1), compared with aggregated nanoparticles (Pd_n).

2.3.1 Solution set-up method. A 100 mg of the catalyst was dispersed in a mixture of 3 mmol of phenylboronic acid, 1 mmol of aryl halide, and 3 mmol of a base, sodium carbonate (Na_2CO_3). The reaction mixture was stirred in 5 ml of water in a two-necked round-bottomed flask using the oil-bath heating method. The product was filtered using a syringe filter and diluted with DCM, thereafter, the reaction progress was monitored by GC-FID. Each variation trial was done in duplicates.

2.3.2 Solid-state set-up method. Phenylboronic acid (3 mmol), aryl halide (1 mmol), in the presence of a base (3 mmol), sodium carbonate (Na_2CO_3), 100 mg of the catalyst, and 0.1 ml of water were mixed. The reactions were conducted in a stainless-steel milling agate grinding jar at 25 Hz using two stainless-steel bearing balls (diameter: 8 mm) for an hour at room temperature. The product was diluted with DCM, filtered, and the progress was monitored by GC-FID.

3. Results and discussion

3.1 Catalyst synthesis and characterization

For the synthesis of ultrasmall Pd clusters, the catalytic metal precursor (potassium tetrachloropalladate) and the support material were mixed at a low weight ratio of 1 : 1000 and 1 : 100 to achieve 0.1 Pd wt% and 1 Pd wt%. Hydrochloric acid was introduced to suppress nucleation, thereby favoring the formation of atomically dispersed Pd species. In addition, the acidic environment influenced the coordination state of the metal precursor, which further stabilized Pd in the early stages of dispersion. For nanoparticles synthesis, higher precursor-to-support ratios of 1 : 100 and 1 : 20 were employed to achieve 1 and 5 Pd wt%, respectively. In this case, emphasis was placed on nucleation and particle growth, achieved through the combined use of urea and sodium borohydride. Urea played a dual role in controlling the pH and facilitating the gradual decomposition of the metal precursor to release ions, which are subsequently reduced to form nanoparticles by sodium borohydride. After complete ball milling, the resulting mixtures were subjected to calcination at 400 °C. The calcination step ensured the removal of residual organics and incomplete decomposition products of the Pd precursor, leading to well-defined Pd small clusters or nanoparticles, depending on the synthesis route. The product was the characterized with different techniques.

Powder X-ray diffraction (p-XRD) analysis was used to track the formation of Pd nanoparticles and to identify the phases of

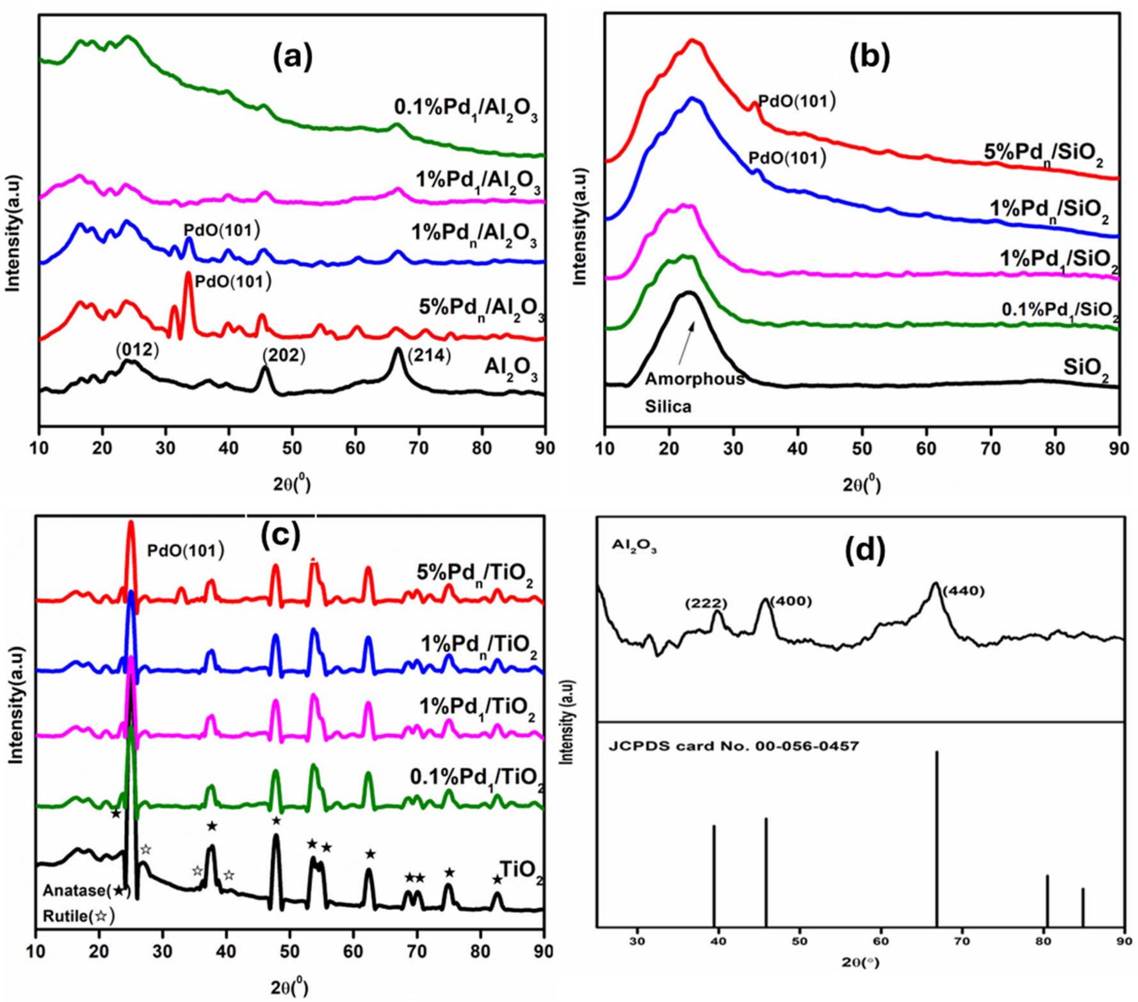

Fig. 1 (a–c) Powder XRD pattern of Pd catalysts on different Pd loadings on different supports and (d) ball milled Al_2O_3.

Table 1 Crystallographic parameters for the synthesized catalysts and comparison with literature

				Lattice parameters			
Entry	Sample	Crystal structure	Space group	*a* (Å)	*b* (Å)	*c* (Å)	References
1	Al$_2$O$_3$	Cubic	$Fd\bar{3}m$	7.9110	7.9110	7.9110	This work
2	1% Pd$_1$/Al$_2$o$_3$	Cubic	$Fd\bar{3}m$	7.9110	7.9110	7.9110	
3	1% Pd$_n$/Al$_2$O$_3$	Tetragonal	$P4_2/mmc$	3.0430	3.0430	5.3370	
4	5% Pd$_n$/Al$_2$O$_3$	Tetragonal	$P4_2/mmc$	3.0430	3.0430	5.3370	
5	TiO$_2$	Tetragonal	$I4_1/amd$	3.8720	3.8720	9.6160	
6	0.1% Pd$_1$/TiO$_2$	Tetragonal	$I4_1/amd$	3.8720	3.8720	9.6160	
7	1% Pd$_1$/TiO$_2$	Tetragonal	$I4_1/amd$	3.8720	3.8720	9.6160	
8	1% Pd$_n$/TiO$_2$	Tetragonal	$I4_1/amd$	3.8720	3.8720	9.6160	
9	5% Pd$_n$/TiO$_2$	Tetragonal	$P4_2/mmc$	3.0430	3.0430	5.3370	
10	γ-Al$_2$O$_3$	Cubic	$Fd\bar{3}m$	7.938	7.938	7.938	32
11	0.2 Au/γ-Al$_2$O$_3$	Cubic	$Fd\bar{3}m$	7.938	7.938	7.938	32

the synthesized catalytic materials. Fig. 1(a) shows the diffractograms of Pd/Al$_2$O$_3$. For 0.1% Pd$_1$/Al$_2$O$_3$ and 1% Pd$_1$/Al$_2$O$_3$ ultrasmall clusters, the diffraction patterns only showed the phases of the support (Al$_2$O$_3$) due to the undetectable amounts of Pd in the overall catalyst materials. Four distinct diffraction peaks at 37.6, 39.4, 45.8, and 66.8° correspond to (311), (222), (400), and (440) planes, respectively.[27] These planes matched with standard ICDD card no 00-056-0457, thus indicating the cubic γ-Al$_2$O$_3$ phases, see Table 1. In the patterns of both the 0.1% Pd$_1$/Al$_2$O$_3$ and 1% Pd$_1$/Al$_2$O$_3$ catalysts, there were no Pd^0 diffraction planes observed, indicating most Pd species are nanoclusters and/or single atoms that are fully dispersed on metal oxide support.[28] The diffraction pattern for 1% Pd$_n$/Al$_2$O$_3$ and 5% Pd$_n$/Al$_2$O$_3$ nanoparticles showed diffraction planes attributable to PdO phases around 33.9°, which correspond to (101) facets, indicating traces of PdO nanoparticles. The PdO peak intensity change between 1% Pd$_n$/Al$_2$O$_3$ and 5% Pd$_n$/Al$_2$O$_3$ materials due to Pd loading, with the higher Pd loading giving higher intensity peaks, signifying the extent of oxidation of Pd metal and the incomplete reduction by borohydride. Also, Table 1 shows that the crystal structure and phases of these catalysts were different from those of supported-ultrasmall clusters, since they have PdO. The formation of PdO instead of zerovalent Pd is expected due to the high calcination temperature during synthesis. Also, PdO is thermodynamically favoured at high temperatures in oxygen-rich environments. It may also be due to Strong Metal–Support Interaction (SMSI). The Pd nanoparticles strongly interact with the supports, leading to stabilization through oxidation.[29] The formation of palladium oxide (PdO) was confirmed through p-XRD pattern from the JCPDS software database (ICDD: 04-005-4781). In Fig. 1(b), the diffraction pattern of Pd/SiO$_2$ is shown. The patterns confirm the presence of amorphous mesoporous silica in all samples. For 0.1% Pd$_1$/SiO$_2$ and 1% Pd$_1$/SiO$_2$ ultrasmall clusters, the diffractograms were similar to the support (SiO$_2$), confirming that the clusters were fully dispersed on the support and the support retained its structural integrity upon deposition. However, the diffractogram of the 5% Pd$_n$/SiO$_2$ and 1% Pd$_n$/SiO$_2$ nanoparticles showed sharp diffraction peaks of PdO located at 33.9° 2θ angles next to the usual SiO$_2$ peak, also indicating the formation of Pd nanoparticles. In Fig. 1(c), the XRD pattern of Pd/TiO$_2$ typically shows characteristic peaks corresponding to both TiO$_2$ anatase and rutile phases. All samples showed diffraction planes at 25.3°; 37.7°; 48°; 53.7°; 55°; 62.6°; 68°,69°; 75.6°; and 82° which is characteristic of the anatase form of TiO$_2$ corresponding to (101), (004), (200), (105), (211) (204), (116), (220), (215), and (224) reflections, respectively.[30] These planes matched the standard ICDD card no 04-011-0664. The diffraction planes seen at 27.8°, 36.2°, and 39.8° are attributed to the rutile form of TiO$_2$, corresponding to (110), (101), and (111) planes, respectively. For 0.1% Pd$_1$/TiO$_2$, 1% Pd$_1$/TiO$_2$, and 1% Pd$_n$/TiO$_2$ catalysts, the XRD patterns were similar to that of TiO$_2$, confirming that the metal loading was too low for detectable amounts and fully dispersed on the support. While 5% Pd$_n$/TiO$_2$ also showed a PdO phase, suggesting the formation of Pd nanoparticles.

Based on the XRD patterns of both sol–gel and ball-milling-synthesized Al$_2$O$_3$ supports exhibit diffraction peaks characteristic of γ-Al$_2$O$_3$ and cubic structure. No additional reflections corresponding to phase transformation of the alumina support were observed, indicating that the mechanochemical synthesis did not induce a detectable phase change of Al$_2$O$_3$ under the applied milling conditions. This might be due to the fact that both sol–gel and ball milling were performed under moderate temperature. Chung *et al.* reported that α-Al$_2$O$_3$ and other phases are mostly formed at 1000 °C.[31]

The electronic structure of the catalysts was analysed by DR UV-Vis between 250–800 nm, as shown in Fig. 2. The UV-Vis diffuse reflectance spectra of each catalyst gave a distinct DRS signature. Comparing these catalysts with their supports helps to understand how different Pd loadings and forms alter the support's electronic structure. In Fig. 2(a), a pure Al$_2$O$_3$ has a wide band gap between $\lambda = 350$ and 370 nm; thereafter, the spectrum stays featureless due to the lack of d-orbitals for electron transfer in the visible region. While TiO$_2$ (Fig. 2(b)) has a clear band gap (∼3.2 eV), showing narrow optical absorbance at $\lambda = 360$ nm. The ultrasmall clusters (Pd$_1$) show distinct spectra from their supports because they are almost atomically dispersed, as shown in Scheme 1. Each Pd cluster behaves like a positively charged unit due to electron withdrawal by the O

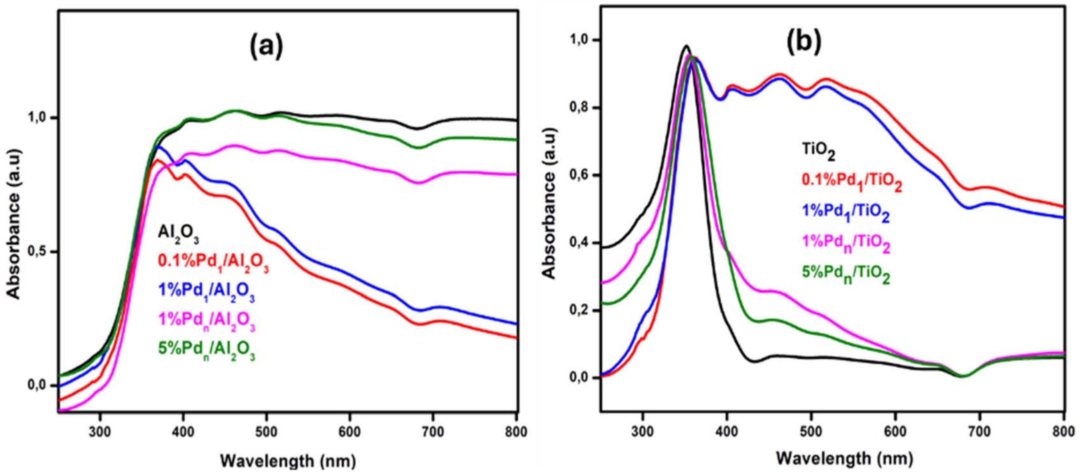

Fig. 2 Shows the UV-Vis diffuse reflectance spectra of (a) Pd/Al_2O_3, and (b) Pd/TiO_2.

atoms of the support. This charge transfer creates a strong metal–support interaction.[33] New discrete states inside the band gap (donor or acceptor levels) arise from Pd–O coordination, leading to a new visible absorption pathway.[34] Nanoparticles are metallic in nature (Pd–Pd metallic bonding). Only surface atoms contact the oxide support, thus bulk atoms interact only with other Pd atoms (as shown in Scheme 1), leading to weaker MSI per atom compared to single atoms or ultrasmall clusters.[35] Optical features mainly come from interband transitions and weak plasmonic effects, not discrete mid-gap states. Hence, the absorption resembles the baseline of the support, with less visible-light enhancement compared to Pd_1 containing catalysts. Weaker MSI means they don't strongly alter the support's band structure.

The FTIR analysis shown in Fig. S1 in the SI was used to monitor the functional groups of metal-oxides upon deposition of different Pd loadings. The catalytic materials exhibit similar FTIR fingerprints. All catalysts displayed bands at $\sim \lambda = 3400\ \text{cm}^{-1}$ attributed to surface-adsorbed water molecules. The band at $\lambda = 2340\ \text{cm}^{-1}$ may be attributed to the stretching vibration of CO_2 molecules from the atmosphere. This typically takes place on the Al_2O_3 surface, due to the presence of basic sites on the γ-Al_2O_3 surface.[36] The Al_2O_3 vibrational and stretching modes were affected by Pd deposition. A visible shift is observed between $\lambda = 1400$ to $1600\ \text{cm}^{-1}$ due to H–O–H bending vibrations of adsorbed water molecules. The sensitive FTIR technique was able to detect even the smallest amount of Pd present on the support, while it was not the case for analysis with P-XRD. The changes in the FTIR of pure alumina after Pd deposition were detected in the range 1400–1600 cm^{-1}. Wherein Pd deposition changes hydroxyl distribution, so comparing Pd/Al_2O_3 to pure Al_2O_3 revealed Pd–OH interactions by reduction in the intensity of the OH bending mode.[37]

The thermogravimetric analysis (TGA) was performed to evaluate the thermal stability of the catalyst with immobilized nanoparticles (1% Pd_n/Al_2O_3 and 5% Pd_n/Al_2O_3), which lost more weight compared to catalysts with immobilized ultrasmall clusters (0.1% Pd_1/Al_2O_3 and 1% Pd_1/Al_2O_3). This implies that the immobilization of ultrasmall clusters brings about better thermal stability than immobilized nanoparticles, as shown in Fig. S2 in the SI. The first weight loss in all catalytic materials between 30 and 180 °C is due to the removal of surface-adsorbed water derived from atmospheric moisture. The weight loss observed between 200 and 600 °C is attributed to removal of organic species and carbon that remain present on the catalyst surface during the synthesis. All the synthesized materials exhibited good thermal stability with less than 10% weight loss at 1000 °C. The high thermal stability of these catalysts means less sintering or particle aggregation in harsh reaction conditions.

The N_2 sorption measurements gave insights into the surface area and porosity of the synthesized catalysts. Fig. 3 and S3 in SI show that all the synthesized catalysts exhibit type IV absorption–desorption isotherms signifying mesoporous nature, but different hysteresis loops were observed. Pd ultrasmall clusters supported on alumina showed H4 type hysteresis loops,[38] signifying narrow slit mesopores limited by the presence of micropores. This might be due to atomically dispersed atoms resulting in strong anchoring or interactions with the support and possibly defect sites, thus altering the porosity.[39,40] SiO_2 and ultrasmall clusters that are supported on silica showed an H1 hysteresis loop, steep uptake near $P/P_0 \approx 0.4$ corresponds to capillary condensation in mesopores. TiO_2 supported clusters and all nanoparticles from all supports showed type IV isotherms with an H3 hysteresis loop, indicating a widely distributed slit-like porous structure.[41] The BET surface areas range between 25.76 ± 1.0 to $296.48 \pm 15\ \text{m}^2\ \text{g}^{-1}$, and the average pore diameters are between 3.56 to 23.5 nm, see Table 2. The surface area and pore volume decreased with increasing metal loading for catalysts on all supports. This phenomenon is due to the blockage of the porous network by Pd particles, partially filling mesopores, thus occupying space.[42] In terms of the surface areas of the supports, the decrease is because the deposited metal occupies the adsorption sites, thus prohibiting N_2 adsorption space. However, for TiO_2-supported catalysts, a different trend was observed. When adding extra small clusters surface area increased, and it was higher than the supports. This might be due to enhanced dispersion. Small clusters of Pd

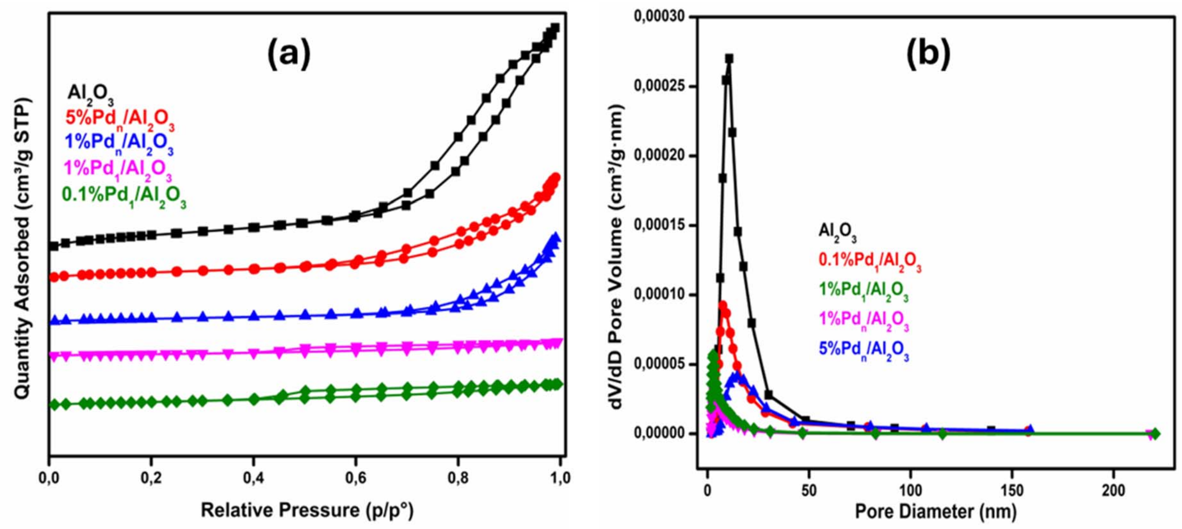

Fig. 3 (a) N_2 adsorption–desorption isotherms of Pd_n-loaded Al_2O_3 and (b) the pore size distribution plots.

may have created new mesoporosity rather than simply blocking pores. Similar results were reported.[43–45] The actual Pd loading was measured by ICP-OES. The Pd content in the 5% Pd_n/Al_2O_3 catalyst is 5.47 wt%, and in the 1% Pd_n/Al_2O_3 catalyst it was found to be 1.12 wt%. These experimentally determined values are not significantly different from the theoretical loadings. This is observed for all other catalysts, as shown in Table 2.

When considering the support materials, the observed decrease in surface area for Al_2O_3 after Pd deposition can be attributed to partial collapse of the porous network caused ball milling technique. This is evidenced by the decreasing pore sizes upon Pd deposition seen in Table 2. On the other hand, TiO_2 and SiO_2 structures appear to be swelling upon deposition of Pd metal. This is seen by increases in both pore volume and pore diameter. Thus, gaseous adsorption can readily take place within the enhanced pore structures. Also, the deposition of Pd within the extended pores enhances the number of active sites.

A comparison of the vibrational or electronic modes of the support before and after metal deposition at different mass loadings was conducted. In Fig. 4(a), the modes of TiO_2 confirm

Table 2 Physicochemical properties of the catalytic materials showing the amount of Pd content, surface area, pore volume, and pore distribution[a]

Entry	Sample	Actual Pd wt% loading	BET surface area (m^2 g^{-1})	V_{Pore} (cm^3 g^{-1})	D_{Pore} (nm)	Pd particle size (nm)	References
1	Al_2O_3	—	103 ± 5.0	0.41	23.54	—	This work
2	5% Pd_n/Al_2O_3	5.47	48.8 ± 2.4	0.02	6.54	4.08 ± 1.8	
3	1% Pd_n/Al_2O_3	1.12	57.3 ± 2.9	0.05	7.91	2.6 ± 0.7	
4	1% Pd_1/Al_2O_3	1.31	52.3 ± 2.6	0.15	8.20		
5	0.1% Pd_1/Al_2O_3	0.17	71.7 ± 3.6	0.21	11.14		
6	TiO_2	—	25.8 ± 1.3	0.38	2.22		
7	5% Pd_n/TiO_2	4.70	22.8 ± 1.1	0.04	13.27	4.6 ± 1.4	
8	1% Pd_n/TiO_2	0,92	20.6 ± 1.0	0.154	11.20	2.1 ± 1.4	
9	1% Pd_1/TiO_2	0.81	34.1 ± 1.7	0.116	3.8		
10	0.1% Pd_1/TiO_2	0.09	36.7 ± 1.8	0.18	10.2		
11	SiO_2	—	288 ± 14	0.35	3.56		
12	5% Pd_n/SiO_2	4.11	38.8 ± 1.9	0.32	7.51		
13	1% Pd_n/SiO_2	0,32	63.0 ± 3.2	0.33	4.61		
14	1% Pd_1/SiO_2	0,64	291 ± 15	0.36	3.9		
15	0.1% Pd_1/SiO_2	0.07	296 ± 15	0.37	4.2		
16	10Ni–2La/SiO_2	10% Ni	292	0.25	0.29		40
17	10Ni–5La/SiO_2	10% Ni	274	0.23	0.29		40
18	Pd_1/ZnO	0.26	18.0	—	—		18
19	AC	—	775	0.39	6.2		46
20	Pd/AC	4.7	747	042	69		46

[a] Actual loading measured by ICP-OES. The average Pd particle size was estimated from the TEM images (Fig. S5 and S7).

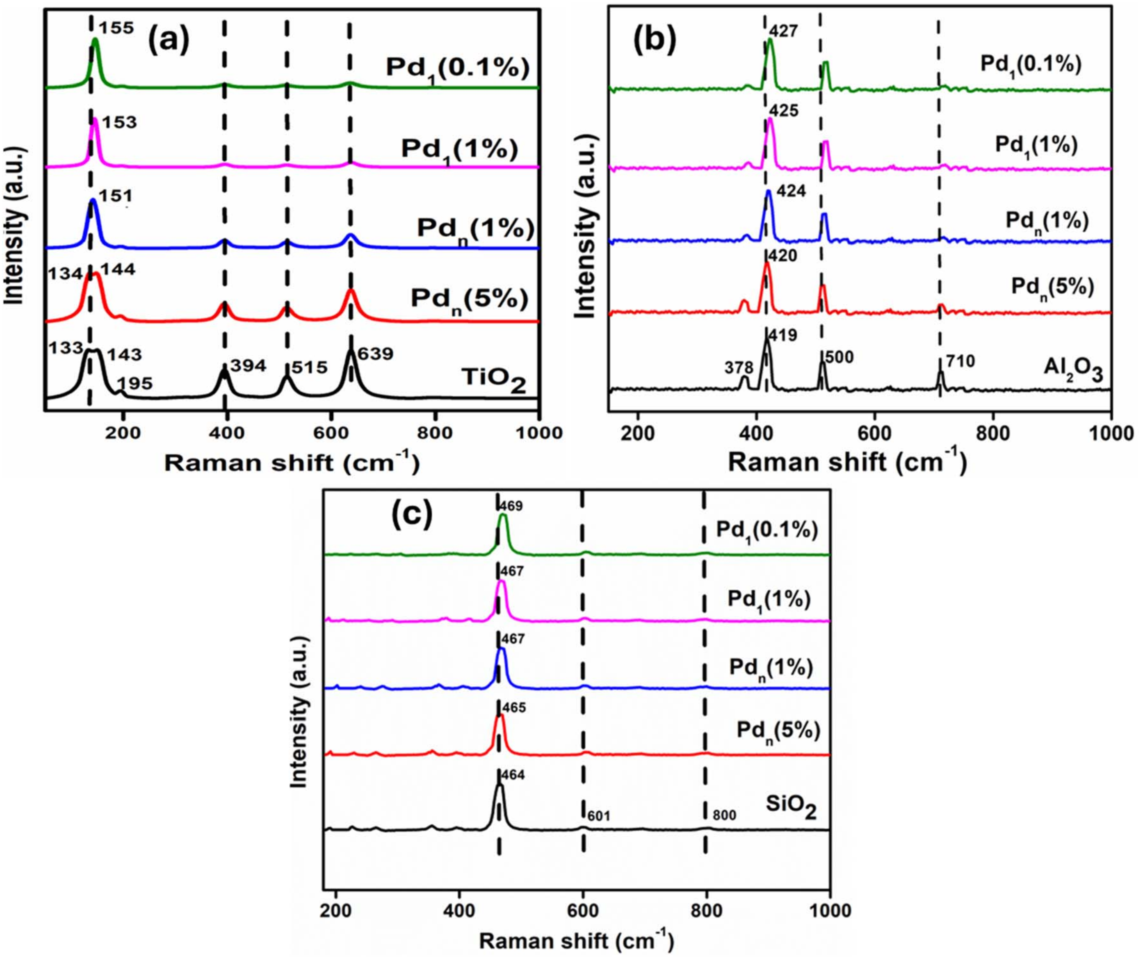

Fig. 4 The Raman spectra of the prepared catalysts supported on (a) TiO_2, (b) Al_2O_3 and (c) SiO_2 showing effect of size on structural changes on the overall catalysts.

that it is mostly in anatase form, as it has six Raman active modes similar to those reported literature.[47] Typical TiO_2 bands appear at 133 (E_g), 143 (E_g), 195 (E_g), 394 (B_{1g}), 515 (A_{1g}), and 639 cm^{-1} (E_g). With a reduction in the metal size loaded, the peaks become less intense, and there is a greater shift of Raman modes, with the band at 133 (E_g) disappearing. After loading 5% Pd_n, the frequency of E_g mode shifted from 143 and 144 cm^{-1} on 5% Pd/TiO_2, and as the metal size is reduced to 0.1% of Pd, the frequency of E_g mode shifted to 143 and 155 cm^{-1} on 0.1% Pd/TiO_2. When comparing our results with literature, we found that this trend has been previously reported for metal-loaded oxide catalysts. The disappearance of the Raman bands after Pd deposition can be attributed to strong metal–support interactions. Pd species anchored on the support surface can reduce the characteristic lattice vibrations of the support resulting in peak broadening or complete disappearance of the corresponding Raman bands. This effect becomes more pronounced as Pd is dispersed on the support surface, even at low metal loadings.[48] The shift of the band at 143 (E_g) is reported to be due to the formation of oxygen vacancies on the support structure. Therefore, the larger Raman shift observed for smaller clusters is likely due to the formation of oxygen vacancies on the support's surface as the size gets reduced.[49] This suggests that a low amount of Pd loading facilitates the generation of oxygen vacancies on the support itself, while a higher amount of Pd loading may tend to block a portion of the oxygen vacancies of the support. As aforementioned, as the metal size is reduced to a smaller cluster, the peaks became less intense at 394 (B_{1g}), 515 (A_{1g}), and 639 cm^{-1} (E_g). The intensity weakens due to Pd–O bonding. Strong Pd–O bonding is ideal in catalysis as it induces oxygen vacancies on the support surface, which act as active adsorption sites for substrates near the metal–support interface. Fig. 4(b) shows the Raman spectra of γ-Al_2O_3 supported catalysts. The Raman signatures, E_g and A_{1g} modes observed, correspond to γ-Al_2O_3. The Raman bands at ~378, 500, and 710 cm^{-1} are assigned to E_g, and the 419 cm^{-1} band is assigned to A_{1g} mode. After loading 5% Pd_n, the frequency of A_{1g} mode shifted from 419 cm^{-1} to 420 cm^{-1}, and as the metal size is reduced to 0.1% of Pd, the frequency of E_g mode shifted from 419 cm^{-1} to 427 cm^{-1}. The peaks become less intense at 378 (E_g) and 419 (A_{1g}), and the intensity weakens due to Pd–O bonding. Fig. 4(c) shows the Raman spectra of SiO_2-supported catalysts. The Raman spectra showed three distinct peaks associated with SiO_2 at ~464, 601, and 800 cm^{-1}. Despite their similar modes with the supports, with the reduction in the Pd loading, the band shifted slightly to higher wavenumbers.

The SEM images and EDX spectra of the as-synthesized catalysts are shown in Fig. 5 and S4 in the SI. All catalysts exhibit rough granular shapes with relatively small particle sizes present on the bulk surface. It was observed that the Pd metal loading influences the size and shape of the supports. The higher the Pd content in the overall catalysts, the smaller the particles in size. Smaller Pd clusters (Pd_1) show larger, irregular shapes and fractured surface morphologies due to their strong interaction with the support. This interaction lowers the surface energy of the support, making it energetically favorable for the support to undergo particle growth or aggregation, which results in larger and more stable particles.[50,51] Such electronic effects at the metal–support interface influence both the stability and the morphology of the overall catalyst. The EDX analysis further confirmed the presence of all the expected elements (Al, Ti, Si, O, and Pd) in the catalysts.

The corresponding size distributions of all the catalytic materials were calculated from HR-TEM images using ImageJ software. The TEM image of the 0.1% Pd_1/Al_2O_3 ultrasmall cluster in Fig. S5(a) revealed small metallic clusters on the surface of the alumina support. As the amount of Pd increased in the metallic cluster to 1% Pd (Fig. S5(b) in SI), clusters were too small or dispersed to give a meaningful distribution. The 1% Pd_n/Al_2O_3 and 5% Pd_n/Al_2O_3 TEM images *n* Fig. S5(c) and (d) in SI showed the presence of Pd nanoparticles. In 1% Pd_n/Al_2O_3 nanoparticles, the histogram shows an average particle size of 2.6 ± 0.7 nm, indicating relatively small and narrowly distributed Pd nanoparticles. The 5% Pd_n/Al_2O_3 nanoparticles are

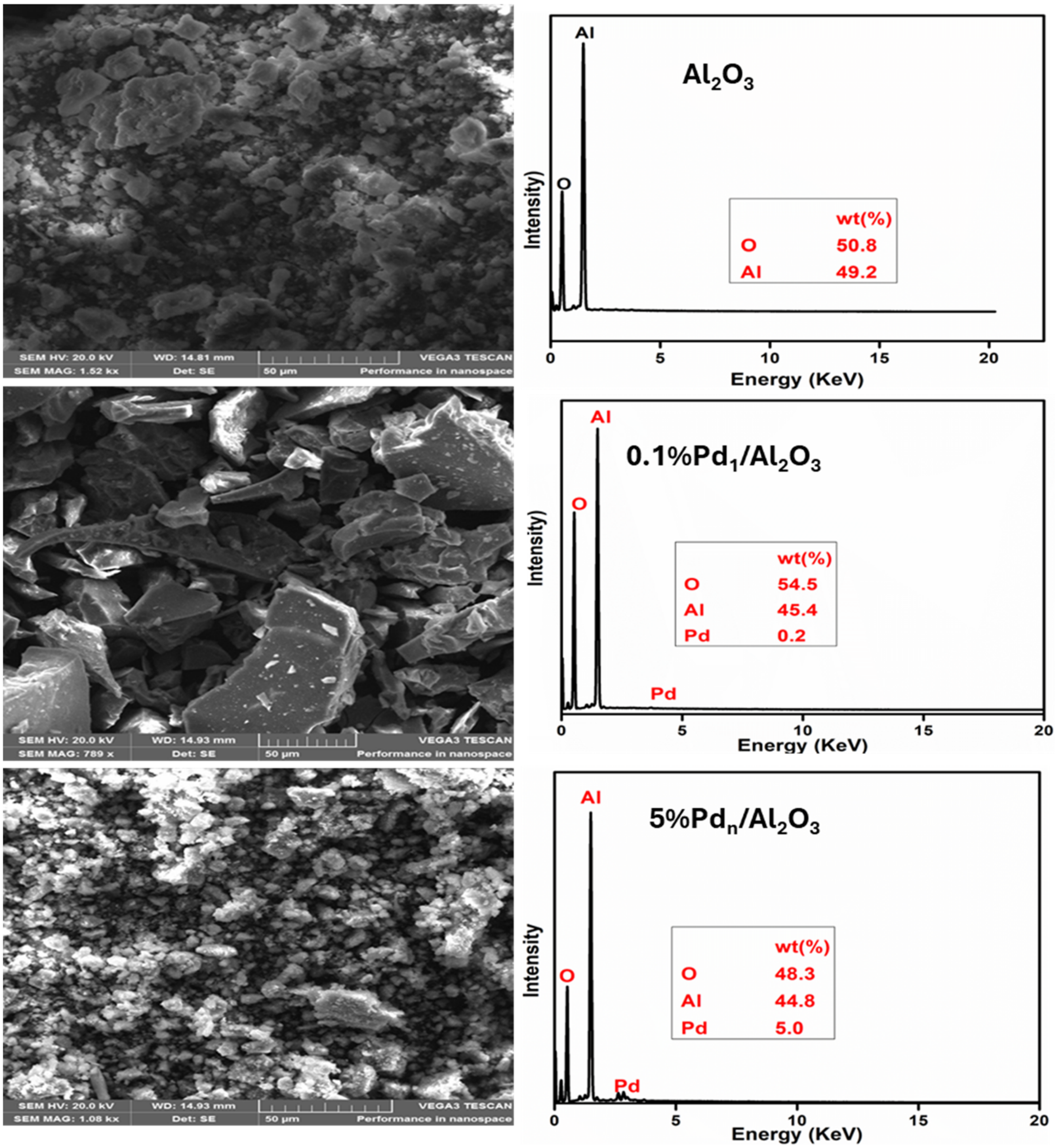

Fig. 5 The SEM images and EDX spectra of Pd/Al_2O_3 catalysts.

formed with an average size of 4.06 ± 1.8 nm, confirming a broader distribution. The growth of Pd nanoparticles with increasing loading is expected due to limited anchoring sites on the Al_2O_3 support and stronger Pd–Pd interactions.

Fig. S6 in SI shows elemental mapping for 0.1% Pd_n/Al_2O_3, showing that Pd, Al, and O atoms were distributed homogeneously on the material's surface. Fig. S7 in SI shows TEM images of TiO_2 catalysts. In Fig. S7(a and b), 0.1% Pd_1/TiO_2 and 1% Pd_1/TiO_2, no larger Pd particles were observed. We confirmed the presence of Pd atoms in 0.1% Pd_1/TiO_2 using elemental mapping (Fig. S8), which showed that Pd atoms are very dispersed, small, and isolated. 1% Pd_n/Al_2O_3 and 5% Pd_n/Al_2O_3 (Fig. S8(c and d) in SI) show the presence of distinct nanoparticles with an average size of 2.1 ± 1.4 nm and with an average size of 4.6 ± 1.4 nm. At higher loading (5%), Pd nanoparticles become more prominent, with larger and more particles. As Pd loading increases, dispersion decreases from atomically dispersed Pd to aggregated nanoparticles, particle size increases, and metal–support interaction weakens, while Pd–Pd interaction strengthens.

Fig. 6 shows the zeta potential as a function of pH for Al_2O_3, TiO_2, and SiO_2 supports. The Al_2O_3 exhibits the highest PZC (PZC = 6.8), while TiO_2 displays an intermediate PZC (PZC = 4.9). In contrast, SiO_2 shows a low PZC (PZC = 3.2), indicating a predominantly acidic surface. In Fig. 7, the 0.1% Pd/Al_2O_3 catalyst exhibits a significantly lower point of zero charge (PZC = 4.8), indicating modification of surface charge properties at low Pd loading. This decrease in PZC suggests strong interaction between Pd atoms and the Al_2O_3 surface. Strong Lewis acidic Al^{3+} sites easily trap Pd atoms, leading to alteration of the surface hydroxyl groups and the formation of more acidic surface sites, such as Pd–O(H) and Pd–O–Al linkages, thus the surface becomes more acidic.[54] Márquez, *et al.* studied DFT and shown that isolated Pd atoms preferentially anchor to tetrahedrally coordinated Al^{3+} sites of Al_2O_3 supports.[54] Therefore, as the loading increases, further changes in the zeta potential profile were observed, which can be attributed to increased surface coverage by PdO species and partial coverage of Al_2O_3 surface sites. These results demonstrate that Pd loading has a strong influence on the surface charge behaviour of Al_2O_3, and that zeta potential measurements are highly sensitive to changes in surface composition and metal–support interactions.

Pyridine probe-FTIR spectroscopy was used to investigate the nature of the acidic sites of the catalysts. Fig. 8(a) shows Al_2O_3 exposed to pyridine with characteristic bands at ~1580 and ~1445 cm^{-1} corresponding to Lewis acidic sites (L), and a band at ~1490 cm^{-1} assigned to combined Lewis–Brønsted acidic sites (L and B), confirming the Lewis acidic nature of the support. In Fig. 8(b) no significant bands were detected in the absence of pyridine, confirming that these features originate from adsorbed pyridine. The Al_2O_3 has more electron accepting sites which come from unsaturated cation (Al^{3+}) than donating sites (H^+). After Pd deposition (0.1–5 wt%), the pyridine-FTIR spectra show similar band positions with no new peaks, indicating that Pd loading does not generate additional acidity but rather interacts with pre-existing acid sites of Al_2O_3. Now comparing 0.1% Pd and 5% Pd loading, it is clear that the

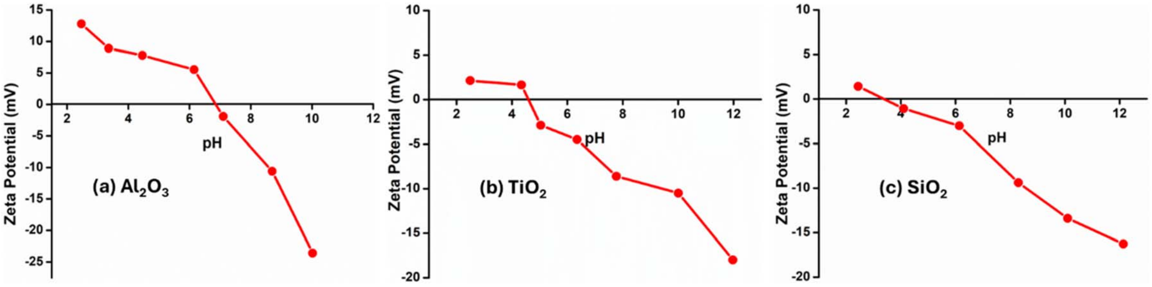

Fig. 6 Surface charge *vs.* pH of (a) Al_2O_3, (b) TiO_2 and (c) SiO_2 supports.

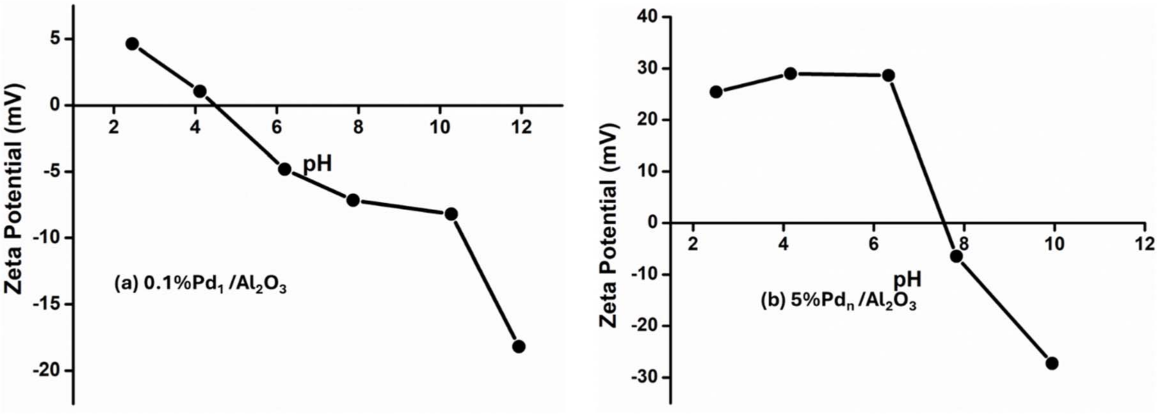

Fig. 7 Surface charge *vs.* pH of (a) 0.1% ultrasmall cluster of Pd and (b) 5% Pd nanoparticles on Al_2O_3.

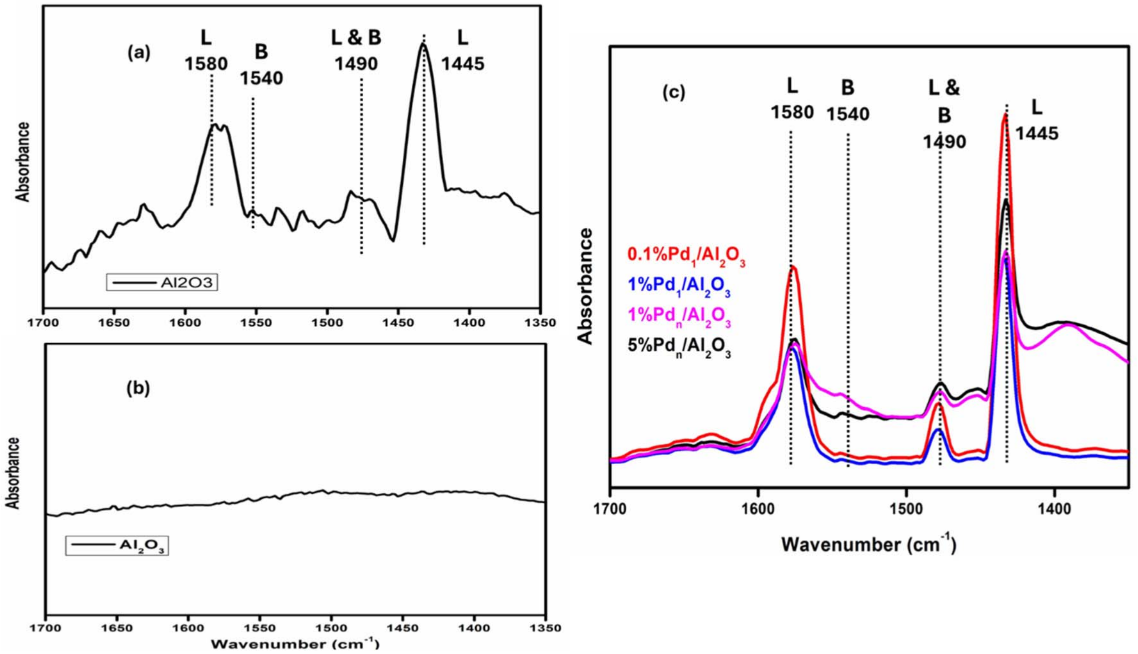

Fig. 8 Pyridine FTIR of the (a) Al_2O_3 support exposed to pyridine, (b) the Al_2O_3 without exposure to pyridine, and (c) Pd-supported catalysts.

intensities became weaker when adding more metal due to metal coverage.

4. Catalytic results and discussion

4.1 Solution-state catalytic properties of Pd/support materials

4.1.1 Influence of support. The supports are not merely inert during the reaction but interact with supported metallic species to create new interfacial effects. Therefore, firstly, a comparison of different supporting metal oxides' effects in the reaction was performed. Fig. 9 shows that the nanoparticles deposited on alumina displayed the highest yield when compared to those deposited on silica and titania. These supported nanoparticles performed in the following order 5% Pd_n/Al_2O_3 (78%) > 5% Pd_n/TiO_2 (72%) > 5% Pd_n/SiO_2 (48%) over 4 hours. The good performance shown by alumina was also reported by Díaz-sánchez *et al.*[52] Also, in their work, they showed through comparison of various Al_2O_3 phases that γ-Al_2O_3 exhibits stronger interaction with Pd than other alumina phases. This leads to uniform dispersion of Pd nanoparticles on γ-Al_2O_3, resulting in better catalytic performance. Suzuki coupling often runs in aqueous or polar solvents with a base, and γ-Al_2O_3 exhibits acid/base properties, rendering it more catalytically active than other supports for this reaction.[53,54] Also, γ-Al_2O_3 has a higher surface area and pore volume than TiO_2 (γ-$Al_2O_3 = 103$ and $TiO_2 = 26\ m^2\ g^{-1}$), leading to enhanced Pd dispersion. Furthermore, the pores act like nanoreactors for

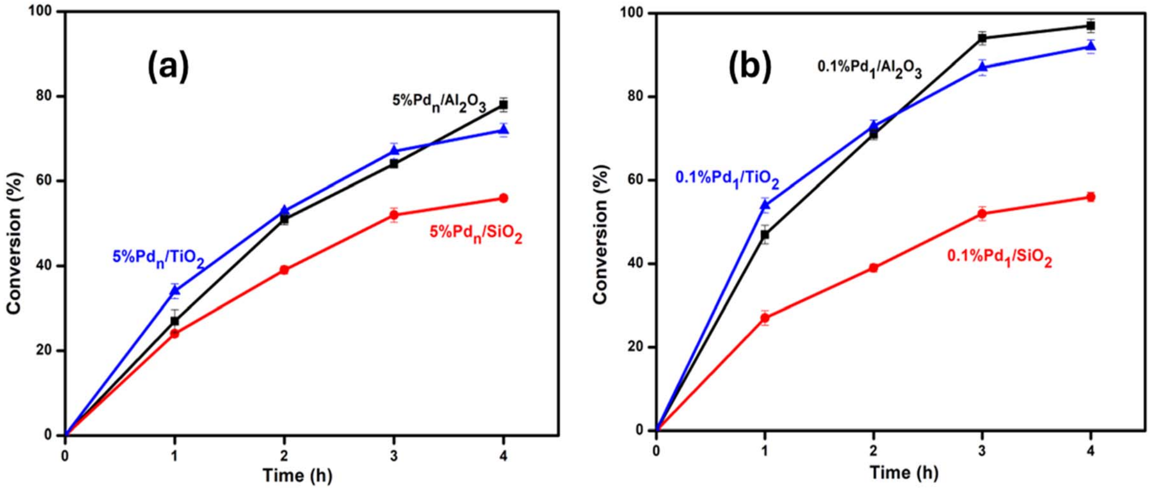

Fig. 9 Effect of different metal-oxide supports with (a) 5% Pd loading in nanoparticles form and (b) 0.1% ultrasmall Pd clusters in Suzuki–Miyaure coupling reaction *via* solution set-up (liquid-H_2O at 80 °C for 4 hours).

carbon–carbon coupling reaction and nanoconfinement for Pd dispersion.

We then compared ultrasmall clusters supported on different metal oxides (0.1% Pd_1/Al_2O_3, 0.1% Pd_1/SiO_2, and 0.1% Pd_1/TiO_2) in the same reaction using the same reaction conditions. The results showed that with the change in catalytic support, the catalytic activity changes. The percentage conversion varies in the following order: 0.1% Pd_1/Al_2O_3 (97%) > 0.1% Pd_1/TiO_2 (92%) > 0.1% Pd_1/SiO_2 (56%) in 4 hours. Again, alumina showed better catalytic activity, as in the case of supported nanoparticles, thus it was chosen as the optimum support for the metal size effect study.

4.1.2 Metal size effects: influence of reduced metal loading on catalytic activity. The influence of the amount of Pd metal in the overall catalyst was evaluated for the reaction between bromobenzene and phenylboronic acid at 80 °C in H_2O and with Na_2CO_3 as a base using alumina as the optimum support. The results revealed that reducing the Pd amount from nanoparticles to ultrasmall clusters increased the percentage conversion of PhBr (Fig. 10(a)). The reaction reached conversions greater than 97% within 4 hours for the metal loading of 0.1% Pd ultrasmall clusters, while the high metal loading of nanoparticles (5%) gave only about 78% conversion after 4 hours. This indicates that the smallest metal catalysts, such as ultrasmall clusters synthesized in this work, are more active in driving the catalytic reaction. While the utilization of metal atoms in nanoparticles is limited to only accessible surface atoms, leading to poor atom utilization, ultrasmall clusters are central to the reduction of precious metals' usage in catalysis and offer a cost-effective route to sustainable catalysis.

The effect of reaction time on catalytic performance is shown in Fig. 10(b). The reaction time was varied from 1 to 4 hours. Up to 3.5 hours, the percentage conversions increased with time. However, at prolonged reaction time, above 3.5 hours, the percentage conversion remains almost the same. This may be due to the irreversible reaction reaching its equilibrium between 3.5 to 4 hours. Therefore, 3.5 hours was selected as the optimum time in the solution set-up.

4.2 Solid-state results and discussion

4.2.1 Solution-assisted catalysis and the effect of reaction time. For liquid–solid interfacial coupling reactions it is known than solvents play a crucial role. For example, solvents are central to catalytic performance by boosting turnover frequency, act as catalytically active metal stabilizers,[55] more especially for the P^0 catalysts in widely applied in Suzuki–Miyaura reactions, and selectivity descriptors.[56] Furthermore, the polarity of the solvent used becomes important in controlling the solubility of the base and stabilizing the reaction transition states.[57] However, in mechanochemical setup, these effects play differently and require careful reconsideration. Solvents act as energy regulators during and after impact of the ball milling process. They also manipulate the surface chemistry of the formation of products at the catalyst interface.

For mechanochemical C–C coupling setup the term solvent will be dropped and replaced by liquid. This is because the liquids are used for a different role unlike as solvents in the liquid–solid interfacial reactions. In this work, the best parameter optimizations from the solution setup were used. The yield decreased significantly because of the optimum liquid effect, water from the solution set-up. Among the liquids evaluated in Table 3, methanol (51% conversion) and isopropanol (33% conversion) performed better than DMF, toluene, and water. This is due to poor binding of alcohols to Pd, thus they do not deactivate the catalyst. While DMF as a Lewis acid binds strongly to Pd, making it a less effective liquid for ball milling technique. This applies to water as well because it interacts strongly with Pd, reducing its effectiveness. Lastly, toluene is an organic liquid, and most organics are known for their lubricating effect. Because of this, toluene reduces the effect of the impact and lowers the effectiveness of the ball milling technique.

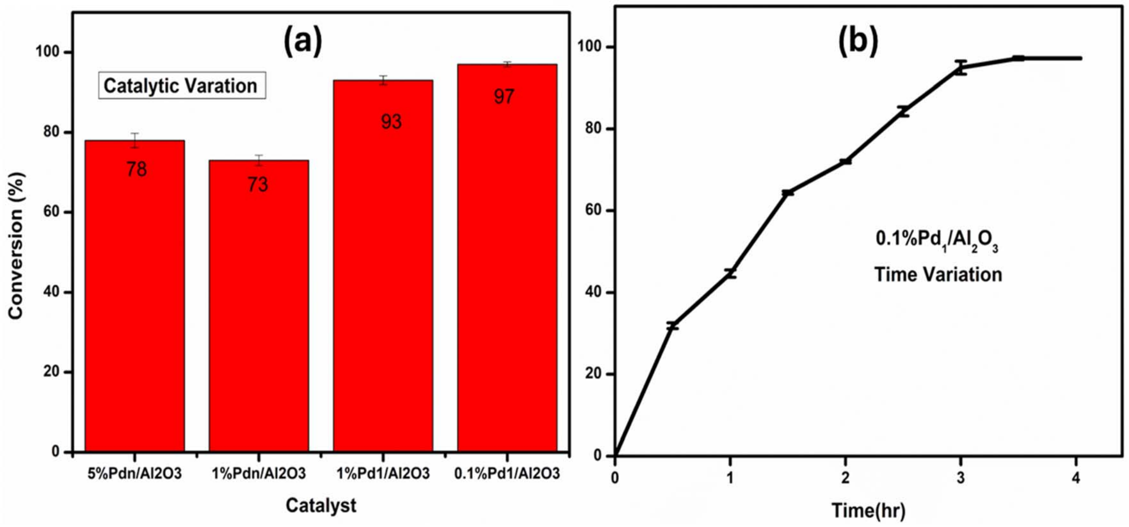

Fig. 10 (a) Comparison of reaction activities of Pd/Al_2O_3 catalysts (catalytic variation) in different metal loading and (b) time effect of 0.1% Pd_1/Al_2O_3 catalyst for the Suzuki coupling reaction.

Table 3 Assisting liquid variation[a]

		Ball milling parameters					
Entry	Liquid (μl)	Time	Speed	Grinding ball size	Temperature	Conversion%	References
1	H_2O	1 h	25 Hz	8 mm	25 °C	6	This work
2	Methanol					51	
3	Toluene					17	
4	Isopropanol					33	
5	DMF					29	
6	H_2O : methanol (1 : 1)					77	
7	H_2O	10 min	30 Hz	5 mm	110 °C	95	58

[a] Reaction conditions: a mixture of phenylboronic acid (3 mmol), bromobenzene (1 mmol), Na_2CO_3 (3 mmol), catalyst (5 mmol%), and liquid (0.1 ml) was milled in a stainless-steel jar at 25 Hz with two stainless-steel balls that were 8 mm in diameter at ambient temperature for 1 hour. Yield determined by GC analysis using an internal standard.

A mixture of methanol and water provided an excellent percentage conversion, 77% as shown in Table 3, entry 6. Different ratios of water and methanol mixture were evaluated as shown in Fig. 11(a). Firstly, the pure liquids induced activity is lower than that of the mixtures. Secondly, a high percentage of methanol in the mixture is less active than when water is in access. Lastly, a mixture consisting of a 1 : 4 methanol : water ratio is the optimum mixture that gives the highest percentage conversion of the substrate (97%). By using this MeOH/H_2O ratio (1 : 4), phenyl boronic acid is 97% converted within an hour at room temperature, which is also the highest conversion obtained for the time variation study shown in Fig. 11(b). The water/methanol mixture gave 77% conversion when mixed in equal amounts. This much improved activity is induced by the synergistic effect of water and methanol on Pd surface chemistry. The high binding affinity of water is countered by the less binding capability of methanol. On the other hand, the phase segregation of water and the reactants is reduced by the presence of methanol. All these factors aid in achieving better catalytic yields.

The atomically dispersed ultrasmall clusters in 0.1% Pd_1/Al_2O_3 gave the highest TON, 5.879×10^5. On the other hand, the nanoparticles in the form of 5% Pd_n/Al_2O_3 exhibited the lowest TON, 1.396×10^4 among the synthesized catalysts. This also shows the potent catalytic nature of the ultrasmall Pd clusters in driving the Suzuki–Miyaura coupling reaction. Furthermore, the highly selective nature of the 0.1% Pd_1/Al_2O_3 catalyst (96.8%) reiterates that the smaller clusters operate more like the atomically dispersed atoms of Pd, thus offering near isolated catalytically active sites that are highly selective. While on the hand, nanoparticles such as 5% Pd_n/Al_2O_3 (94.8%) have facets that offer different adsorption energies, thus leading to less selective route to product formation. Eqn (3)–(5) were used to calculate turnover number (TON), percentage selectivity, and percentage yield, respectively. Table 4 shows the catalytic turnovers of the synthesized catalysts.

$$\mathrm{TON} = \frac{\mathrm{moles}_{\mathrm{of\ \ product}}}{\mathrm{moles}_{\mathrm{of\ \ metal(Pd)}}} \quad (3)$$

$$\%\ \mathrm{Selectivity} = \frac{\mathrm{moles}_{\mathrm{Biphenyl\ \ in\ \ product}}}{\mathrm{moles}_{\mathrm{PhBr\ in\ product}}} \times 100 \quad (4)$$

$$\%\ \mathrm{Biphenyl\ \ yield} = \frac{\mathrm{moles}_{\mathrm{Biphenyl\ \ in\ \ product}}}{\mathrm{moles}_{\mathrm{PhBr(initial)}}} \times 100 \quad (5)$$

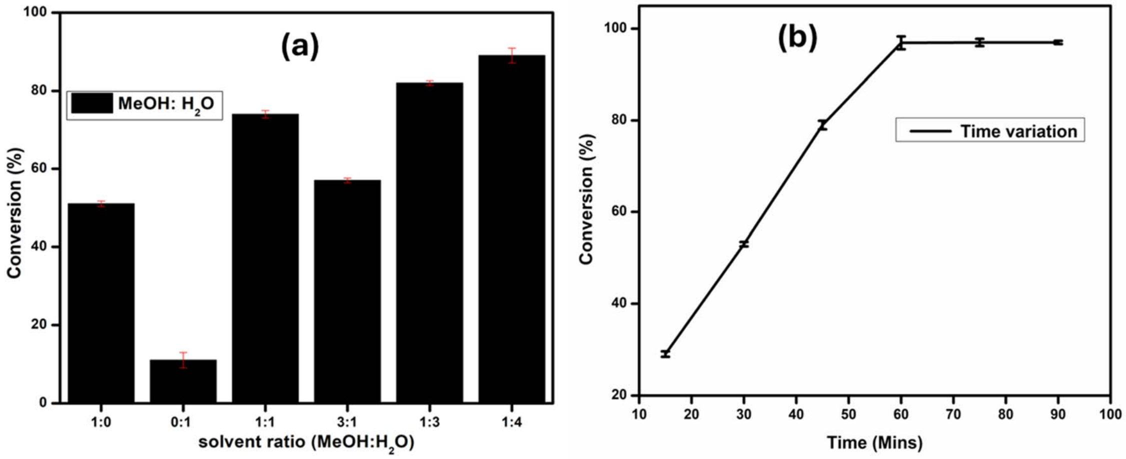

Fig. 11 (a) Liquid variation and (b) time effect.

Table 4 Catalytic activity parameters (conversion, selectivity, yield, and TON) for Pd/Al_2O_3 catalysts

Entry	Catalyst	No. of moles of Pd (mmol)	Conversion (%)	Selectivity (%)	Yield	TON	Reference
1	0.1% Pd_1/Al_2O_3	1.597×10^{-3}	97.0	96.8	93.9	5.879×10^5	This work
2	1% Pd_1/Al_2O_3	0.0123	84.4	97.3	82.1	6.675×10^4	
3	1% Pd_n/Al_2O_3	0.0105	71.1	97.1	69.0	6.571×10^4	
4	5% Pd_n/Al_2O_3	0.0514	75,7	94.8	71.76	1.396×10^4	
5	Pd–Co–Mg–Fe-CHT	0.009	—	—	93	4.261×10^4	59
6	Pd/CNS	0.45% w/w	—	—	95	1.2×10^2	60
7	Pd/AC	4.7	—	—	80	222	46
8	Ac–Pd	7.63	—	—	69	192	61

5. Proposed Suzuki–Miyaura reaction mechanism

The Suzuki–Miyaura reaction follows a three-step pathway involving (i) oxidative addition (dissociative adsorption of aryl halide), (ii) transmetalation (dissociative adsorption of alkali-activated phenylboronic acid), and (iii) reductive elimination (coupling of two phenyl groups). A proposed reaction mechanism is summarized in Scheme 2. The PdO supported on Al_2O_3 was first activated *in situ* under basic conditions and reduced to form Pd^0, the active catalytic species. Thereafter, the bromobenzene (electrophile) undergoes oxidative addition and is coordinated to Pd^0, increasing palladium's oxidation state, forming a R–Pd(II)–X complex. The boronic acid is activated by a base ion to form a phenyl anion, which then transfers its aryl group to Pd(II) in the transmetalation step. Then, the two aryl groups on Pd(II) not only couple to form the biaryl product but also form Pd(0) to complete the catalytic cycle.

6. ^{1}H NMR spectra of the coupling products of the Suzuki–Miyaura reaction

To confirm the catalytic product, ^{1}H NMR was used. All proton signals fall in the aromatic region (7.2–7.6 ppm), and the total

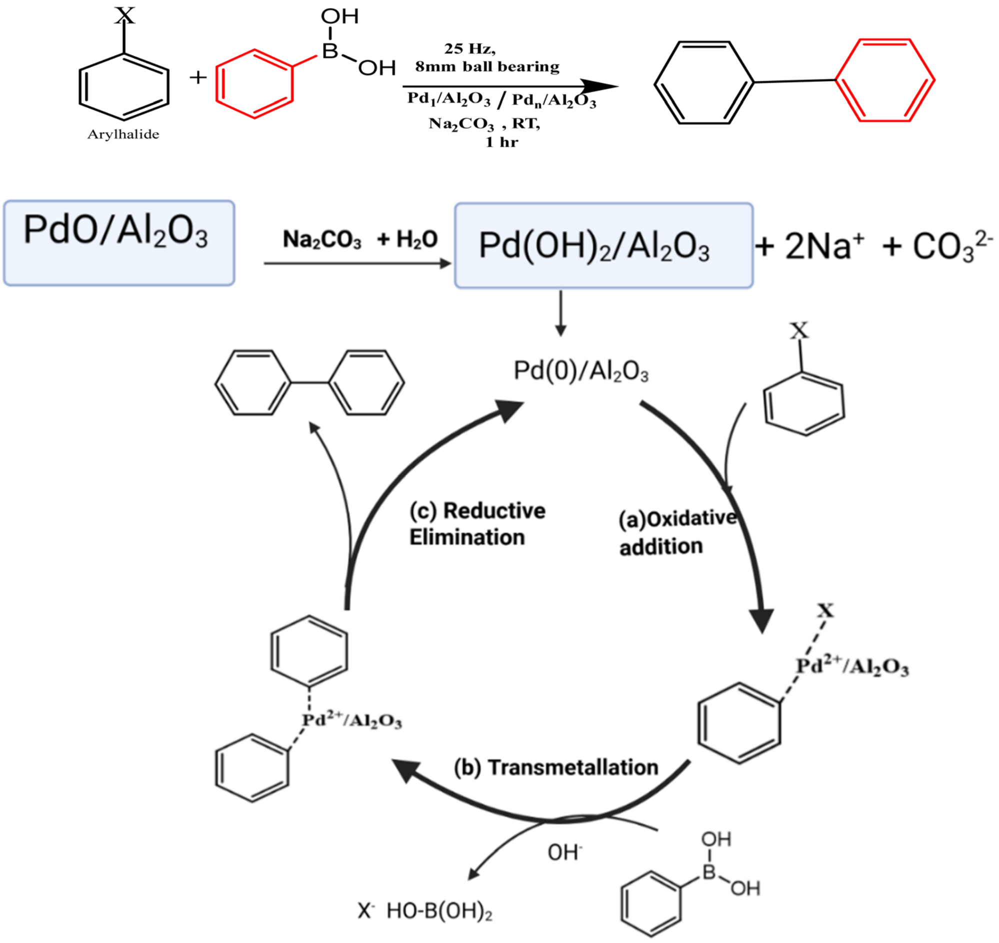

Scheme 2 Reaction mechanism of heterogeneous Pd/Al_2O_3-catalysed Suzuki–Miyaura reaction.

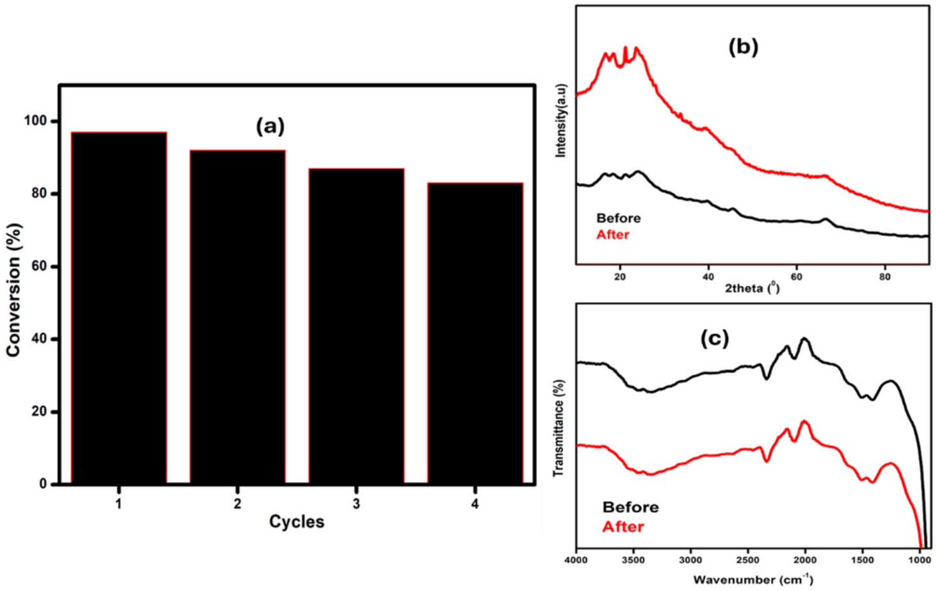

Fig. 12 Recyclability studies, (a) conversion *versus* number of cycles, (b) P-XRD of the catalyst (before and after 3 cycles), and (c) FTIR results before and after reaction.

integration of ten protons was observed, indicating an aromatic system with ten hydrogens, a biphenyl. From the ^{1}H NMR (500 MHz, $CDCl_3$) results, δ: 7.65 (d, J = 7.41 Hz 4H), 7.34 (t, J = 9.1 Hz, 4H), 7.32 (t, J = 7.15 Hz 2H), only three prominent signals for all ten protons were observed, indicative of a symmetrical arrangement with two equivalent aromatic rings. The chemical shifts at δ 7.56, d, $J \approx 7.4$ Hz, are 4H likely to be the *ortho* protons labelled as c in (Fig. S9), a doublet with integration 4H fits two *ortho* protons on each ring that are magnetically equivalent by symmetry. The chemical shifts at δ 7.31, t, $J = 9.1$ Hz, 4H, are likely to be the *meta* protons and are labelled b in Fig. S9. The expected usual ^{3}J values are $\sim$7–8 Hz, but here 9.1 Hz was observed, which is a bit larger than usual. This is reported to happen because of spectral overlap or solvent impurities, and looking at Fig. S9, there is an overlap. Integration 4H matches two *meta* protons per ring. δ 7.25, t, $J = 7.15$ Hz, 2H, likely the *para* protons, integration 2 protons match one para proton labelled a proton per ring. This analysis confirms the successful catalytic synthesis of biphenyl using a Suzuki–Miyaura reaction.

7. Catalytic recyclability studies

The recycled catalysts were reused for four catalytic cycles, as shown in Fig. 12(a). After four cycles, no significant reduction in reaction yields was observed. Furthermore, the FTIR spectrum of the spent catalyst after the fourth cycle, shown in Fig. 12(c), was obtained and compared to that of the fresh catalyst, with both spectra appearing similar to each other. Likewise, the PXRD of the spent catalyst was also obtained and compared with the fresh catalyst, and it was observed that the recycled catalyst did not undergo any significant changes in its structure Fig. 12(b), indicating good catalytic stability. The slight decrease in the conversion may be due to a mass loss during recycling.

8. Conclusion

In this study, we demonstrated the use of the liquid-assisted grinding (LAG) ball milling method as an effective alternative route for the synthesis of low-loading Pd catalysts. The results revealed that at reduced metal loadings, palladium formed ultrasmall clusters with discrete energy levels that were more uniformly dispersed across the support surface. The catalytic activity of these catalysts was systematically compared across different supports. Notably, the ultrasmall Pd clusters exhibited enhanced performance in the Suzuki–Miyaura coupling reaction under both solution-phase and solid-state conditions. Furthermore, our findings highlighted that the solid-state setup offered superior efficiency compared to the solution-phase system, achieving faster reaction rates and higher substrate conversion at room temperature, particularly when assisted by a water–methanol mixture.

Author contributions

Zizo Feketshane: performed the experiments, analyzed the data, and drafted the manuscript. Ndzondelelo Bingwa and Banele Vatsha: conceptualization, writing – review, and editing of the manuscript. All authors have read and agreed on the final version of the manuscript.

Conflicts of interest

The authors declare no conflict of interest.

Data availability

Data will be made available on request.

Supplementary information (SI): description of characterization methods, FTIR, TGA, TEM, SEM, EDX, elemental mapping, and NMR spectra. See DOI: https://doi.org/10.1039/d6ra00004e.

Acknowledgements

The authors would like to thank the National Research Foundation of South Africa (grant UIDs: 141079 and 138186) for financial support. Also, we would like to express gratitude to the Research Center for Synthesis and Catalysis of the University of Johannesburg for financial support. Furthermore, we would like to thank the Institute of Catalysis and Energy Solutions of the University of South Africa for resources to carry out this project.

References

1 E. Fernández, M. A. Rivero-Crespo, I. Domínguez, P. Rubio-Marqués, J. Oliver-meseguer, L. Liu, M. Cabrero-antonino, R. Gavara, J. C. Hernández-Garrido, M. Boronat, A. Leyva-pe and A. Corma, Base-Controlled Heck Suzuki and Sonogashira Reactions Catalyzed by Ligand-Free Platinum or Palladium Single Atom and Sub- Nanometer Clusters, *J. Am. Chem. Soc.*, 2019, **141**(5), 1928–1940, DOI: 10.1021/jacs.8b07884.

2 M. Hosseini-Sarvari and Z. Razmi, Palladium supported on zinc oxide nanoparticles as efficient heterogeneous catalyst for Suzuki-miyaura and hiyama reactions under normal laboratory conditions, *Helv. Chim. Acta*, 2015, **98**, 805–818, DOI: 10.1002/hlca.201400331.

3 J. Almond-thynne, D. C. Blakemore, C. Pryde and A. C. Spivey, Chemical Science Site-selective Suzuki – Miyaura coupling of heteroaryl halides – understanding the trends for pharmaceutically important classes, *Chem. Sci.*, 2017, 40–62, DOI: 10.1039/c6sc02118b.

4 W. Shi, Y. Niu, S. Li, L. Zhang, Y. Zhang, G. A. Botton, Y. Wan and B. Zhang, Revealing the Structure Evolution of Heterogeneous Pd Catalyst in Suzuki Reaction *via* the Identical Location Transmission Electron Microscopy, *ACS Nano*, 2021, **15**, 8621–8637, DOI: 10.1021/acsnano.1c00486.

5 M. Abroudi, A. Tadjarodi, Z. Rezvani, A. Mollahosseini and S. M. S. Ahmadian, Synthesis and characterization of Pd nanoparticles anchored on MIL 101(Cr) as a novel and recyclable catalyst for the Suzuki cross-coupling reactions, *Microporous Mesoporous Mater.*, 2022, **331**, 111599, DOI: 10.1016/j.micromeso.2021.111599.

6 Y. Lou, J. Xu, Y. Zhang, C. Pan, Y. Dong and Y. Zhu, Metal-support interaction for heterogeneous catalysis: from nanoparticles to single atoms, *Mater. Today Nano*, 2020, **12**, 100093, DOI: 10.1016/j.mtnano.2020.100093.

7 A. A. Melvin, K. Illath, T. Das, T. Raja, S. Bhattacharyya and C. S. Gopinath, M-Au/TiO2 (M = Ag, Pd, and Pt) nanophotocatalyst for overall solar water splitting: role of interfaces, *Nanoscale*, 2015, **7**, 13477–13488, DOI: 10.1039/c5nr03735b.

8 C. Wang, Y. Li, C. Zhang, X. Chen, C. Liu, W. Weng, W. Shan and H. He, A simple strategy to improve Pd dispersion and enhance Pd/TiO2 catalytic activity for formaldehyde oxidation: The roles of surface defects, *Appl. Catal. B Environ.*, 2021, **282**, 119540, DOI: 10.1016/j.apcatb.2020.119540.

9 Q. Zhang, T. Li, X. T. Min, S. X. Li, X. Jiang, Q. Zhang, Y. Li, X. Yan, R. Feng, F. Yang, W. Zhou, X. Hu, B. Qiao and Z. Ni, Size-Activity Relationship of TiO2-Supported Pt Nanoparticles in Hydrogenation Reactions, *Inorganics*, 2025, **13**, 1–14, DOI: 10.3390/inorganics13060186.

10 Z. Feng, X. Chen and X. Bai, Catalytic dehydrogenation of liquid organic hydrogen carrier dodecahydro-N-ethylcarbazole over palladium catalysts supported on different supports, *Environ. Sci. Pollut. Res.*, 2020, **27**, 36172–36185, DOI: 10.1007/s11356-020-09698-w.

11 Y. Li, Y. Zhang, K. Qian and W. Huang, Metal-Support Interactions in Metal/Oxide Catalysts and Oxide-Metal Interactions in Oxide/Metal Inverse Catalysts, *ACS Catal.*, 2022, **12**, 1268–1287, DOI: 10.1021/acscatal.1c04854.

12 J. Xia, L. Dong, X. Liu, R. Chernikov, M. Shakouri, Y. Hu, Y. Guo, J. Wang, K. Song, P. Hu, Y. Wang and H. Wang, Identifying the Activity Origin of a Single-Atom Au 1/Nb 2 O 5 Catalyst for Hydrodeoxygenation of Methylcatechol: A Stable Substitutional Au + Site, *ACS Catal.*, 2023, 6093–6103, DOI: 10.1021/acscatal.3c00513.

13 S. Ji, Y. Chen, X. Wang, Z. Zhang, D. Wang and Y. Li, Chemical Synthesis of Single Atomic Site Catalysts, *Chem. Rev.*, 2020, **120**, 11900–11955, DOI: 10.1021/acs.chemrev.9b00818.

14 H. Wei, X. Li, B. Deng, J. Lang, Y. Huang, X. Hua and Y. Qiao, Rapid synthesis of Pd single - atom/cluster as highly active catalysts for Suzuki coupling reactions, *Chin. J. Catal.*, 2022, **43**, 1058–1065, DOI: 10.1016/S1872-2067(21)63968-2.

15 W. Li, Z. Guo, J. Yang, Y. Li, X. Sun, H. He, S. Li, and J. Zhang, *Advanced Strategies for Stabilizing Single-Atom Catalysts for Energy Storage and Conversion*, Springer Nature Singapore, 2022, DOI: 10.1007/s41918-022-00169-z.

16 H. Wang and J. Lu, A Review on Particle Size Effect in Metal-Catalyzed Heterogeneous Reactions, *Chin. J. Catal.*, 2020, **38**, 1422–1444, DOI: 10.1002/cjoc.202000205.

17 D. Sharma, D. Sajwan, S. Mishra, A. Gouda, P. Mittal, P. Choudhary, B. P. Mishra, S. Kumar and V. Krishnan, Tailoring catalysis at the atomic level: trends and breakthroughs in single atom catalysts for organic transformation reactions, *Nanoscale Horiz.*, 2024, **10**, 423–459, DOI: 10.1039/d4nh00479e.

18 X. He, Y. Deng, Y. Zhang, Q. He, D. Xiao, M. Peng, Y. Zhao, H. Zhang, R. Luo, T. Gan, H. Ji and D. Ma, Mechanochemical Kilogram-Scale Synthesis of Noble Metal Single-Atom Catalysts, *Cell Rep. Phys. Sci.*, 2020, **1**, 100004, DOI: 10.1016/j.xcrp.2019.100004.

19 Y. Hu, B. Li, C. Yu, H. Fang and Z. Li, Mechanochemical preparation of single atom catalysts for versatile catalytic applications: A perspective review, *Mater. Today*, 2023, **63**, 288–312, DOI: 10.1016/j.mattod.2023.01.019.

20 L. Yang, Z. Pan and Z. Tian, Mechanochemical Synthesis of Solid Catalysts and Application in Catalytic Reaction,

ChemCatChem, 2024, **16**(10), 1–13, DOI: 10.1002/cctc.202301519.

21 P. F. M. De Oliveira, R. M. Torresi and P. H. C. Camargo, Challenges and opportunities in the bottom-up mechanochemical synthesis of noble metal nanoparticles, *J. Mater. Chem. A*, 2020, **8**, 16114–16141, DOI: 10.1039/d0ta05183g.

22 M. Al-Naji, A. M. Balu, A. Roibu, M. Goepel, W.-D. Einicke, R. Luquec and R. Gläser, Mechanochemical preparation of advanced catalytically active bifunctional Pd-containing nanomaterials for aqueous phase hydrogenation, *Catal. Sci. Technol*, 2015, **5**, 2085–2091, DOI: 10.1039/c4cy01174k.

23 K. Kubota, Y. Pang, A. Miura and H. Ito, Redox reactions of small organic molecules using ball milling and piezoelectric materials, *Science*, 2019, **366**, 1500–1504, DOI: 10.1126/science.aay8224.

24 R. Tang, X. Dong, J. Sheng, S. Xi, L. Zhang and F. Dong, Single-metal catalytic sites *via* high-throughput mechanochemistry enable selective and efficient CO2 photoreduction, *Appl. Catal. B Environ.*, 2022, **316**, 121661, DOI: 10.1016/j.apcatb.2022.121661.

25 T. M. Rabalao, B. Ndaba, A. Roopnarain and B. Vatsha, A facile plant and chemical-mediated mechanosynthesis of α-Fe $_2$ O $_3$ nanoparticles, *RSC Adv.*, 2025, **15**, 16792–16798, DOI: 10.1039/D5RA02321A.

26 P. Ying, J. Yu and W. Su, Liquid-Assisted Grinding Mechanochemistry in the Synthesis of Pharmaceuticals, *Adv. Synth. Catal.*, 2021, **363**, 1246–1271, DOI: 10.1002/adsc.202001245.

27 F. Wang, J. Ma, G. He, M. Chen, C. Zhang and H. He, Nanosize Effect of Al2O3 in Ag/Al2O3 Catalyst for the Selective Catalytic Oxidation of Ammonia, *ACS Catal.*, 2018, **8**, 2670–2682, DOI: 10.1021/acscatal.7b03799.

28 T. Gan, Q. He, H. Zhang, H. Xiao, Y. Liu, Y. Zhang, X. He and H. Ji, Unveiling the kilogram-scale gold single-atom catalysts *via* ball milling for preferential oxidation of CO in excess hydrogen, *Chem. Eng. J.*, 2020, **389**, 124490, DOI: 10.1016/j.cej.2020.124490.

29 D. J. Pérez-martínez, E. M. Gaigneaux and S. A. Giraldo, Applied Catalysis A : General Improving the selectivity to HDS in the HDT of synthetic FCC naphtha using sodium doped amorphous aluminosilicates as support of CoMo catalysts, *Appl. Catal., A*, 2012, **421–422**, 48–57, DOI: 10.1016/j.apcata.2012.01.036.

30 S. K. M. Jose, Dielectric functionalities of anatase phase titanium dioxide nanocrystals synthesized using water-soluble complexes, *Appl. Phys. A*, 2017, **123**, 1–10, DOI: 10.1007/s00339-017-1121-0.

31 J. Y. Chung, S. Kodama and H. Sekiguchi, Preparation of a Pd/Al_2O_3 Catalyst with Microwave-Induced Plasma Jet Irradiation under Atmospheric Pressure, *Nanomaterials*, 2019, 1734, DOI: 10.3390/nano9121734.

32 F. Saira, N. Firdous, R. Qureshi and A. Ihsan, Preparation and catalytic evaluation of Au/γ-Al2O3nanoparticles for the conversion of 4-nitrophenol to 4-aminophenol by spectrophotometric method, *Turk. J. Chem.*, 2020, **44**, 448–460, DOI: 10.3906/KIM-1910-21.

33 X. Shi, Z. Wen, Q. Gu, L. Jiao, H. Jiang, H. Lv, H. Wang, J. Ding, M. P. Lyons, A. Chang, Z. Feng, S. Chen, Y. Lin, X. Xu, P. Du, W. Xu, M. Sun, Y. Li, B. Yang and T. Zhang, Metal – support frontier orbital interactions in single-atom catalysis, *Nature*, 2025, **640**, 668–675, DOI: 10.1038/s41586-025-08747-z.

34 U. Kerketta and A. B. Tesler, Single-Atom Co-Catalysts Employed in Titanium Dioxide Photocatalysis, *Catalysts*, 2022, 1–40, DOI: 10.3390/catal12101223.

35 B. Xia, Y. Zhang, J. Ran, M. Jaroniec and S. Z. Qiao, Single-Atom Photocatalysts for Emerging Reactions, *ACS Cent. Sci.*, 2021, **7**, 39–54, DOI: 10.1021/acscentsci.0c01466.

36 V. H. T. Nguyen, M. N. Nguyen, T. T. Truong, T. T. Nguyen, H. V. Doan and X. N. Pham, One-Pot Preparation of Alumina-Modified Polysulfone-Graphene Oxide Nanocomposite Membrane for Separation of Emulsion-Oil from Wastewater, *J. Nanomater.*, 2020, 1–12, DOI: 10.1155/2020/9087595.

37 N. Xiang, X. Han, Y. Bai, Q. Li, J. Zheng and Y. Li, Size e ff ect of γ -Al 2 O 3 supports on the catalytic performance of Pd/γ -Al 2 O 3 catalysts for HCHO oxidation, *Mol. Catal.*, 2020, **494**, 111112, DOI: 10.1016/j.mcat.2020.111112.

38 Z. Zou, M. Meng and Y. Zha, Surfactant-Assisted Synthesis, Characterizations, and Catalytic Oxidation Mechanisms of the Mesoporous MnO_x - CeO_2 and Pd/MnO_x - CeO_2 Catalysts Used for CO and C_3H_8 Oxidation, *J. Phys. Chem. C*, 2010, 468–477, DOI: 10.1021/jp908721a.

39 C. Chen, W. Wang, Q. Ren, R. Ye, N. Nie, Z. Liu, L. Zhang and J. Xiao, Impact of preparation method on nickel speciation and methane dry reforming performance of Ni/SiO2 catalysts, *Front. Chem.*, 2022, **10**, 1–11, DOI: 10.3389/fchem.2022.993691.

40 A. R. Aghamiri, S. M. Alavi, A. Bazyari and A. Azizzadeh Fard, Effects of simultaneous calcination and reduction on performance of promoted Ni/SiO2 catalyst in steam reforming of propane, *Int. J. Hydrogen Energy*, 2019, **44**, 9307–9315, DOI: 10.1016/j.ijhydene.2019.02.128.

41 S. Ntshibongo, M. Maumela and N. Bingwa, Synthesis, characterization and catalytic evaluation of supported catalysts (PdNPs/TiO2, PdNPs/Al2O3, PdNPs/SiO2) for esterification of levulinic acid to levulinate esters, *Inorg. Chem. Commun.*, 2022, **146**, 110101, DOI: 10.1016/j.inoche.2022.110101.

42 C. Wang, A. Wang, Z. Yu, Y. Wang, Z. Sun, V. M. Kogan and Y. Y. Liu, Aqueous phase hydrogenation of furfural to tetrahydrofurfuryl alcohol over Pd/UiO-66, *Catal. Commun.*, 2021, **148**, 106178, DOI: 10.1016/j.catcom.2020.106178.

43 X. Li, K. Sun, Y. Chen and Y. Yuan, Study on the Gas-Chromic Character of Pd/TiO2 for Fast Room-Temperature CO Detection, *Molecules*, 2024, **29**, 1–12, DOI: 10.3390/molecules29163843.

44 Y. Guo, Y. Huang, B. Zeng, B. Han, M. Akri, M. Shi, Y. Zhao, Q. Li, Y. Su, L. Li, Q. Jiang, Y. T. Cui, L. Li, R. Li, B. Qiao and T. Zhang, Photo-thermo semi-hydrogenation of acetylene on Pd1/TiO2 single-atom catalyst, *Nat. Commun.*, 2022, **13**, 2648, DOI: 10.1038/s41467-022-30291-x.

45 Y. Deligiannakis, V. Tsikourkitoudi, P. Stathi, K. Wegner, J. Papavasiliou and M. Louloudi, PdO/Pd0/TiO2Nanocatalysts Engineered by Flame Spray Pyrolysis: Study of the Synergy of PdO/Pd0on H2Production by HCOOH Dehydrogenation and the Deactivation Mechanism, *Energy Fuels*, 2020, **34**, 15026–15038, DOI: 10.1021/acs.energyfuels.0c02399.

46 M. M. A. Soliman, A. F. Peixoto, A. P. C. Ribeiro, M. N. Kopylovich, E. C. B. A. Alegria and A. J. L. Pombeiro, Mechanochemical preparation of Pd(II) and Pt(II) composites with carbonaceous materials and their application in the Suzuki-Miyaura reaction at several energy inputs, *Molecules*, 2020, **25**, 2951, DOI: 10.3390/molecules25122951.

47 L. Chu, Z. Qin, J. Yang and X. Li, Anatase TiO2 Nanoparticles with Exposed {001} Facets for Efficient Dye-Sensitized Solar Cells, *Sci. Rep.*, 2015, **5**, 1–10, DOI: 10.1038/srep12143.

48 K. H. Leong, H. Y. Chu, S. Ibrahim and P. Saravanan, Palladium nanoparticles anchored to anatase TiO 2 for enhanced surface plasmon resonance-stimulated, visible-light-driven photocatalytic activity, *Beilstein J. Nanotechnol.*, 2015, **6**, 428–437, DOI: 10.3762/bjnano.6.43.

49 Z. Li, M. Zhang, X. Dong, S. Ji, L. Zhang, L. Leng, H. Li, J. H. Horton, Q. Xu and J. Zhu, Strong electronic interaction of indium oxide with palladium single atoms induced by quenching toward enhanced hydrogenation of nitrobenzene, *Appl. Catal. B Environ.*, 2022, **313**, 121462, DOI: 10.1016/j.apcatb.2022.121462.

50 L. M. Prates, J. W. D. M. Carneiro and M. T. D. M. Cruz, Influence of the metal – support and metal – metal interactions on Pd nucleation and NO adsorption in a - Pd4/γ - Al_2O_3 (110D) model, *J. Mol. Model.*, 2022, **3**, DOI: 10.1007/s00894-022-05374-7.

51 J. Lee, E. Jeong, D. Gun, J. Szanyi and J. Hun, Morphology and size of Pt on Al 2 O 3 : The role of specific metal-support interactions between Pt and Al 2 O 3, *J. Catal.*, 2020, **385**, 204–212, DOI: 10.1016/j.jcat.2020.03.019.

52 M. Díaz-sánchez, D. Díaz-garcía, S. Prashar and S. Gómez-ruiz, Palladium nanoparticles supported on silica , alumina or titania : greener alternatives for Suzuki – Miyaura and other C – C coupling reactions, *Environ. Chem. Lett.*, 2019, **17**, 1585–1602, DOI: 10.1007/s10311-019-00899-5.

53 T. W. Chang Liu and R. Hou, Role of Acid Sites and Surface Hydroxyl Groups in Isophthalonitrile Hydrogenation Catalyzed by Supported Ni-Co Catalysts, *RSC Adv.*, 2015, **5**, 26465–26474, DOI: 10.1039/C5RA01007A.

54 A. M. Márquez and J. F. Sanz, Adsorption of Pd atoms on γ-Al_2O_3: a density functional study of metal–support interactions, *Appl. Surf. Sci.*, 2004, **238**, 82–85, DOI: 10.1016/j.apsusc.2004.05.188.

55 A. D. L. De Boisjan, C. Allemann and L. Fadini, Impact of Solvent and Their Contaminants on Pd/C Catalyzed Suzuki-Miyaura Cross-Coupling Reactions, *Helv. Chim. Acta*, 2021, **104**(6), e2100035, DOI: 10.1002/hlca.202100035.

56 E. K. Reeves, O. R. Bauman, G. B. Mitchem and S. R. Neufeldt, Solvent Effects on the Selectivity of Palladium-Catalyzed Suzuki-Miyaura Couplings, *Isr. J. Chem.*, 2020, 406–409, DOI: 10.1002/ijch.201900082.

57 T. Mandal and K. Panu, $PdCl_2(PPh_3)_2$ Catalyst for Suzuki – Miyaura Reaction, *J. Synth. Chem.*, 2024, **3**(2), 135–148, DOI: 10.22034/jsc.2024.483973.1082.

58 K. Kubota, E. Baba, T. Seo, T. Ishiyama and H. Ito, Palladium-catalyzed solid-state borylation of aryl halides using mechanochemistry, *Beilstein J. Org. Chem.*, 2022, **18**, 855–862, DOI: 10.3762/bjoc.18.86.

59 Z. Dong, P. Gao, Y. Xiao, J. Chen and W. Wang, Pd – Co Nanoparticles Supported on Calcined Mg – Fe Hydrotalcites for the Suzuki – Miyaura Reaction in Water with High Turnover Numbers, *Catalysts*, 2019, **9**(12), 10612019, DOI: 10.3390/catal9121061.

60 L. Riva, G. Nicastro, M. Liu, C. Battocchio, C. Punta and A. Sacchetti, Pd-Loaded Cellulose NanoSponge as a Heterogeneous Catalyst for Suzuki – Miyaura Coupling Reactions, *Gels*, 2022, **8**(12), 789, DOI: 10.3390/gels8120789.

61 M. A. Andrade and M. D. R. S. Martins, New Trends in C – C Cross-Coupling Reactions: The Use of Unconventional Conditions, *Molecules*, 2020, **25**(23), 5506, DOI: 10.3390/molecules25235506.